Supplementary Information

A Microfluidic Chip with Serpentine Channel Enabling High-throughput Cell Separation Using Surface Acoustic Waves

Shupeng Ning,[a,b] Shuchang Liu,[a,b] Yunjie Xiao,[c] Guanyu Zhang,[a,b] Weiwei Cui[a,b,*] and Mark Reed[d,*]

[a] *School of Precision Instrument and Opto-Electronics Engineering, Tianjin University, Tianjin 300072, China*

[b] *State Key Laboratory of Precision Measuring Technology & Instruments, Tianjin 300072, China*

[c] *School of Life Sciences, Tianjin University, Tianjin 300072, China*

[d] *School of Engineering and Applied Sciences, Yale University, New Haven CT 06511, United States*

Device setup

The sample flow and sheath flow driven by syringe pumps were injected into PDMS microchannel, and the samples after separation were collected through sterile tubing in centrifuge tubes (blue path). The required signal was generated by a signal generator and amplified by a RF power amplifier , then the signal was divided into two channels and applied to two interdigital transducers, respectively (black path). Observation and image collection were performed on the microscopic imaging platform. A lamp source excited fluorescent tags
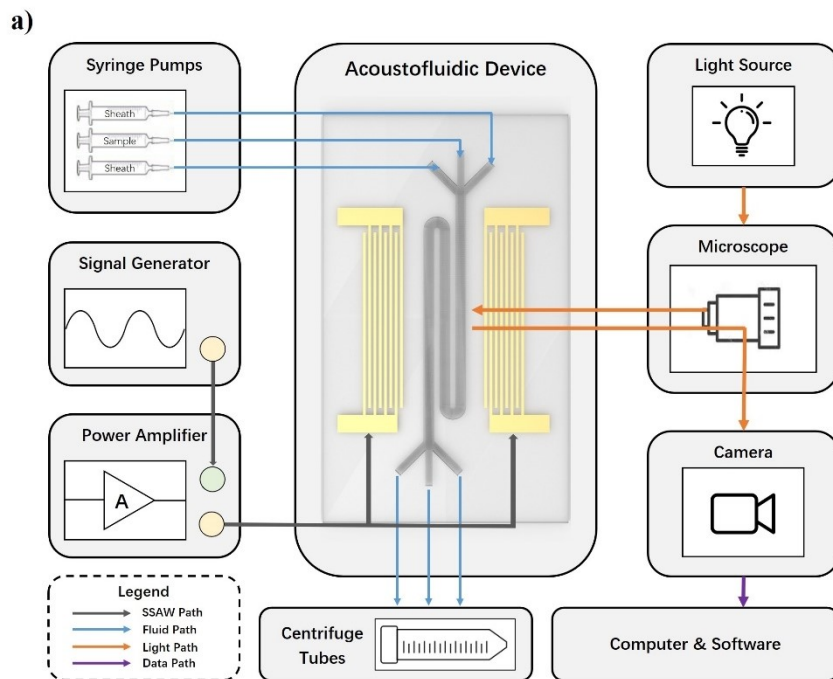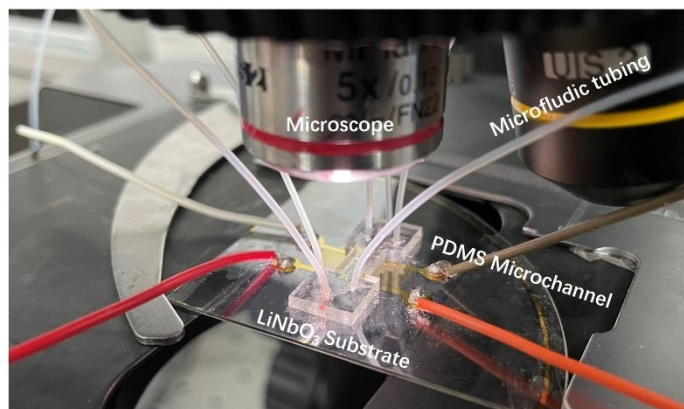
Figure S1. Diagram of device setup and separation workflow (a) Instrumentation schematic for cell separation, and data collection. **(b)** Side view of the experimental setup.

on polystyrene microspheres and *E. coli* (blood cells were observed in bright field) through the microscope objective, and images (sequences) were captured via camera (orange path). The collected images were further processed and analyzed on PC (purple path).

Table S1 Summary for separation techniques using microfluidic tools.

Separation technique	Separation principle	Sample composition	Throughput/ flow rate	Target cell recovery	Target cell Purity	Reference
Passive separation techniques:						
Pillar array structure	Size, deformability	Diluted whole blood	1000 µm/s	~99%	~99%	[1]
Hydrodynamic filtration	Size	Leukocytes and RBCs	20 µL/min	—	increased ~29-fold	[2]
Inertia focusing	Size, shape, deformability	*E. coli* mixed with diluted whole blood	15 µL/min	62%	99.87%	[3]
Active separation techniques:						
SSAW	Size, density, compressibility	*E. coli* and PBMCs	0.5 µL/min	—	95.56%	[4]
taSSAW	Size, density, compressibility	*E. coli* and RBCs	1 µL/min	>98%	>97%	[5]
TSAW	Size, density, compressibility	3 & 10 µm particles	25 µL/h	Close to 100%	Close to 100%	[6]
SSAW+TSAW	Size, density, compressibility	RBCs & U87 glioma cells	0.3µL/min	—	90%	[7]
DEP	Size, polarizability	*E. coli* mixed with diluted whole blood	0.5 µL/min	87.2%	Close to 100%	[8]
Magnetophoresis	Size, magnetic susceptibility	*E. coli* and RBCs	25 µL/h	78%	>99%	[9]
Optical	Size, refractive index, polarizability	Polymer and silica spheres	30 µm/s	—	—	[10]
Serpentine-SSAW	Size, density, compressibility	*E. coli* and RBCs	2.6 µL/min	97.50%[*]	98.02%[*]	This work

*In this work, the cell recovery and purity were calculated without considering cells did not belong to either *E.coli* domain or RBCs domain.

Fluorescent image details

In this paper, we used fluorescent polystyrene particles and GFP-*E. coli* to demonstrate separation performance of the acoustofluidic device, and the distribution of particles/cells in serpentine microchannel was semi-quantitatively analyzed by microscopic fluorescent image sequences. Meanwhile, we stacked and averaged the consecutive image sequences, and the
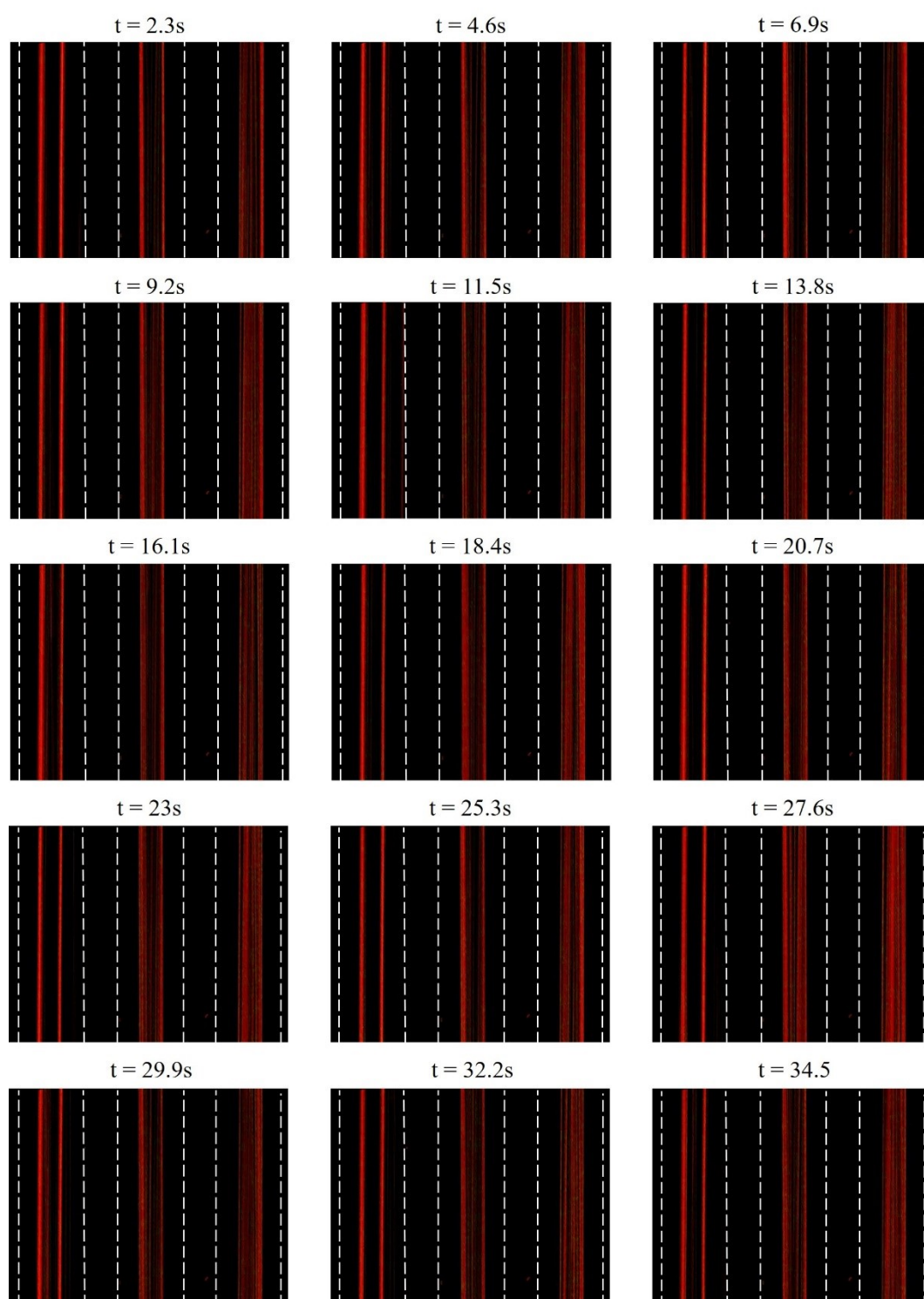
Figure S2. Fluorescent image sequence for 5 μm red fluorescent polystyrene particles in serpentine microchannel. The exposure time was 2.3 s.

results were shown in Figure 3(a)(b) and Figure 4(b). Each frame of fluorescent images was illustrated as follow.
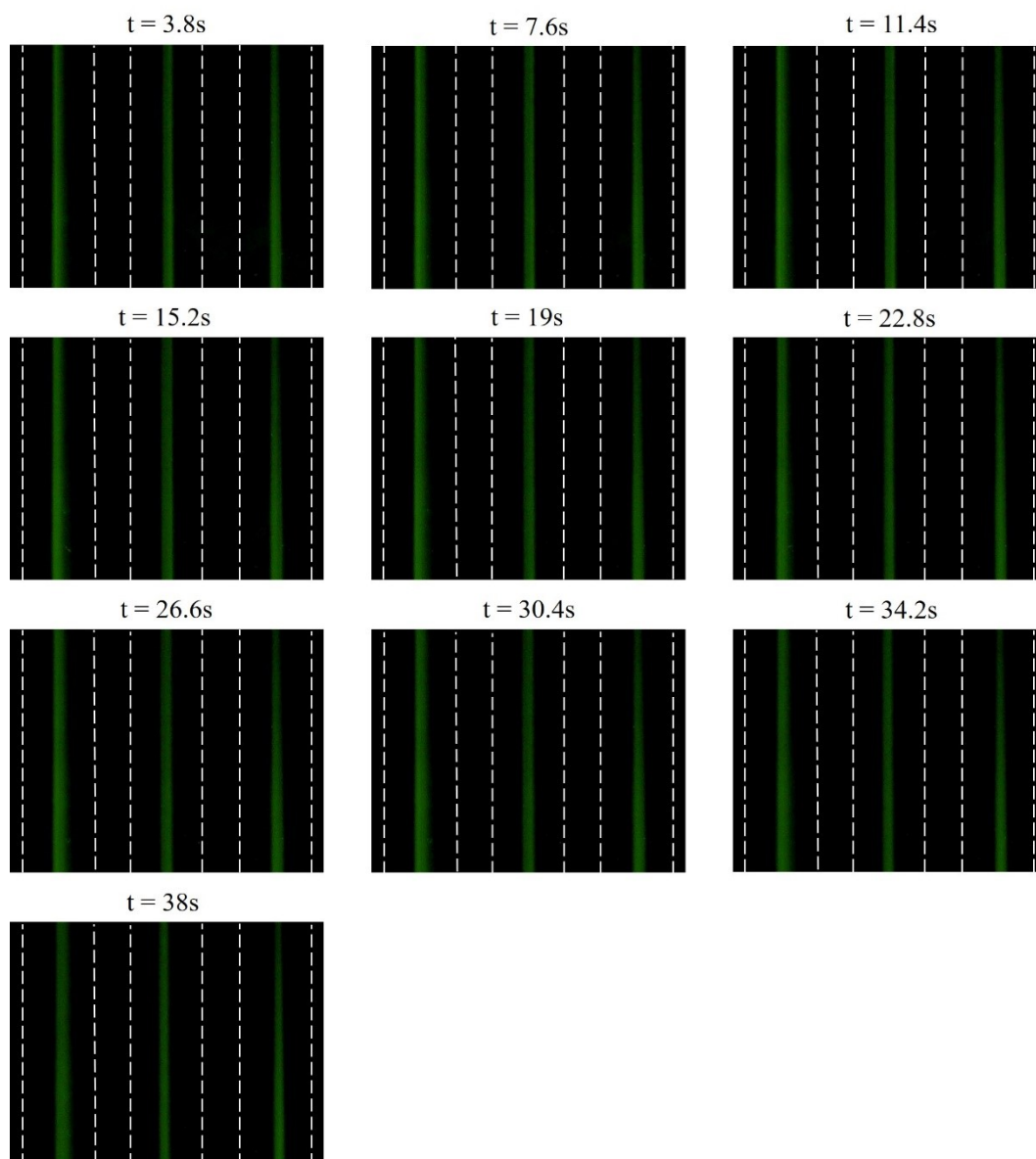
Figure S3. Fluorescent image sequence for 1 μm green fluorescent polystyrene particles in serpentine microchannel. The exposure time was 3.8 s.

t = 2.7s   t = 5.4s   t = 8.1s   t = 10.8s   t = 13.5s

t = 16.2s   t = 18.9s   t = 21.6s   t = 24.3s   t = 27s

t = 29.7s   t = 32.4s
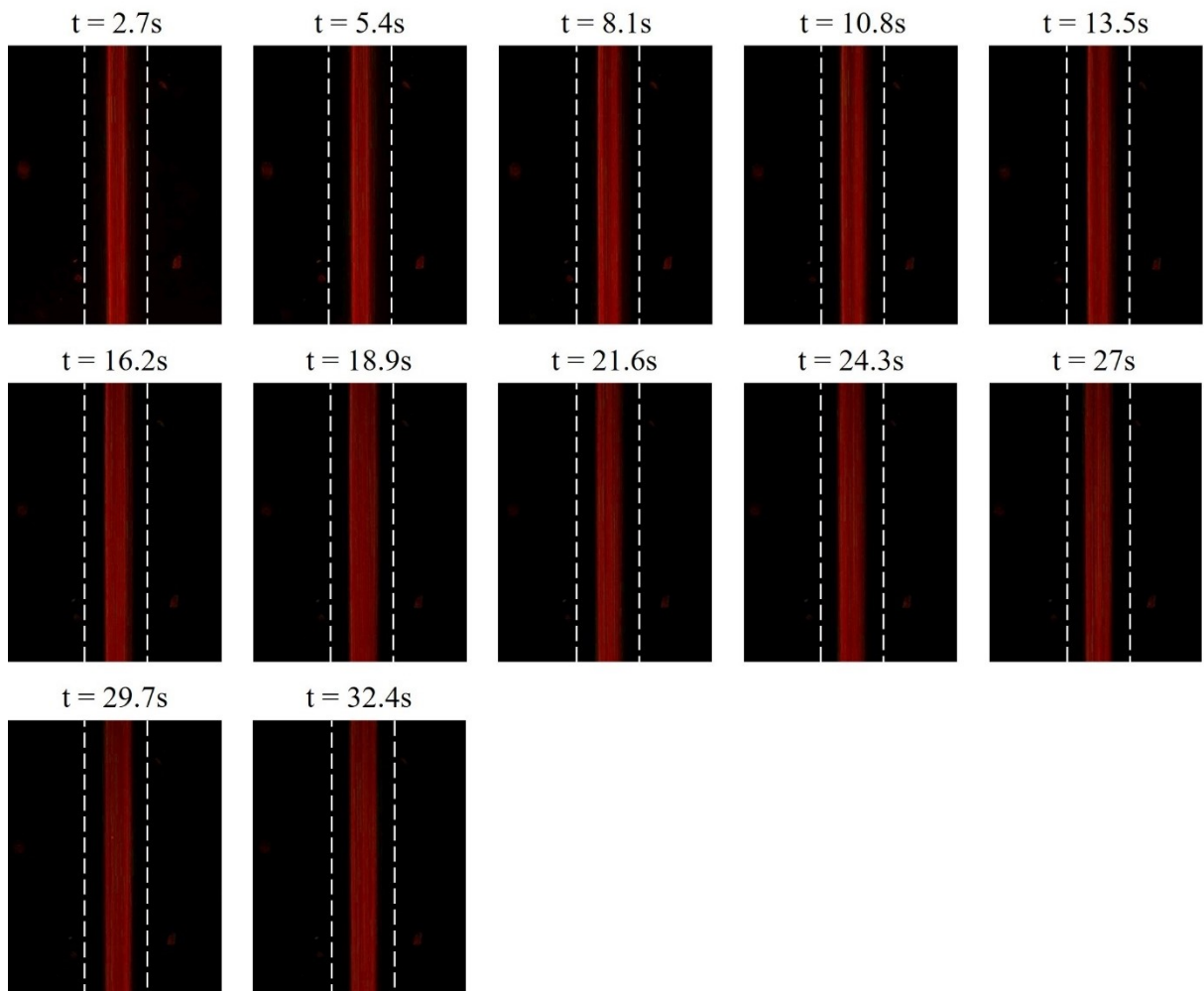
Figure S4. Fluorescent image sequence for 5 μm red fluorescent polystyrene particles in single-channel device. The exposure time was 2.7 s.
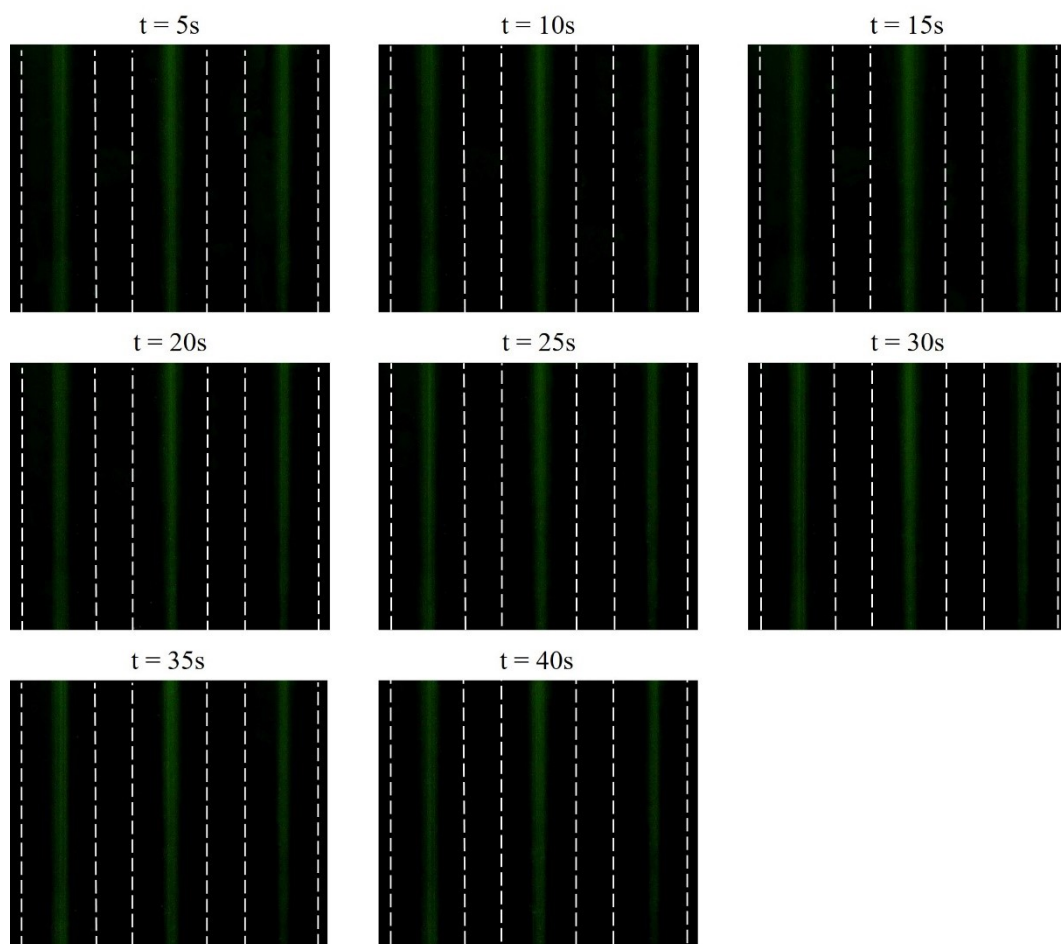
Figure S5. Fluorescent image sequence for GFP-expressing *E. coli* in serpentine microchannel. The exposure time was 5 s.

The serpentine microfludic design with three subsections needs two 180° turns. In our design, these two turns were located outside the acoustic separation area to avoid that particles or cells deviated from previous trajectories when they flowed through the turns. Besides, no obvious mixing between sample flow and sheath flow was observed at the turns whether SSAW field exited or not.
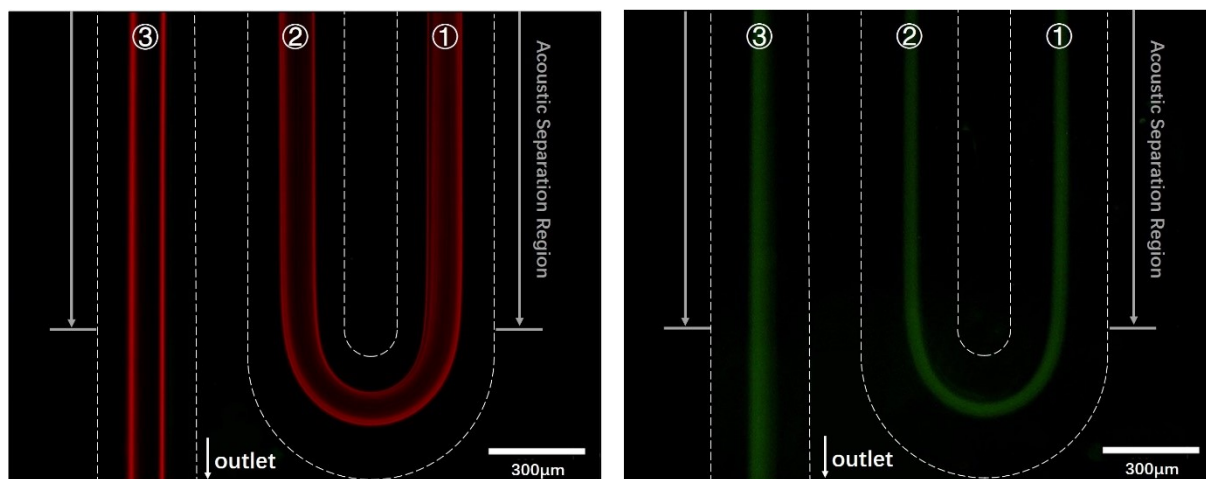
Figure S6. Distribution of particles (5 µm with red fluorescence and 1 µm with green fluorescence) at the corners of serpentine microchannel while SAW was on.

RBCs and E. coli domain in flow cytometry scatter plot

Before further analysis for cell population components in samples, the domains for RBCs and *E. coli* in 2D flow cytometry scatter plot was determined by the testing results of pure cell samples. As shown in Figure S3, *E. coli* and RBCs could be clearly distinguished by their difference on side scatter (SSC-A) and forward scatter (FSC-A). The pattern of RBCs was relatively concentrated, with more than 99% RBCs were included by an elliptical domain; and the most of *E. coli* (95.2%) were contained in a drop-shaped domain while the pattern of *E. coli*
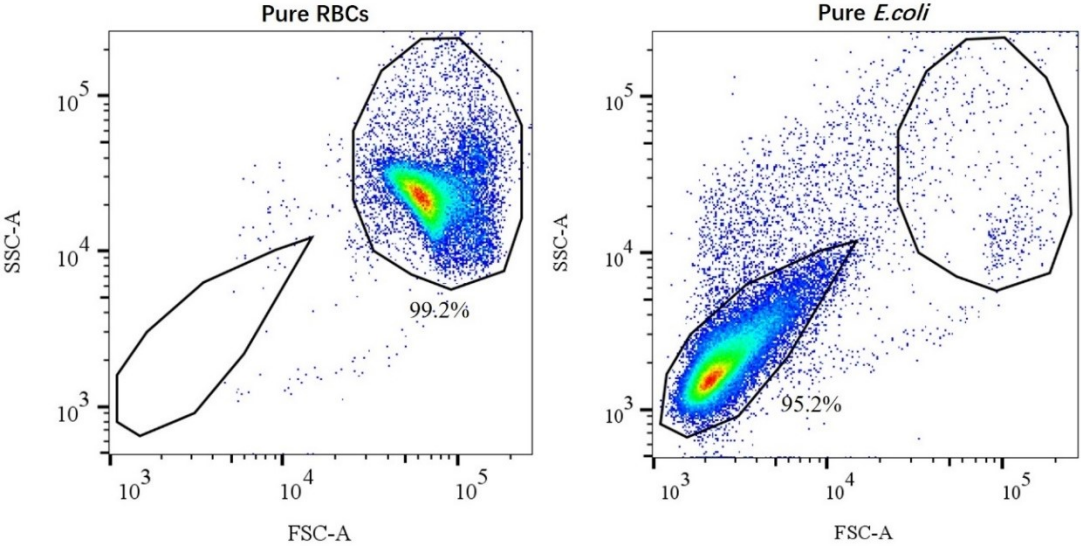
Figure S7. Flow cytometry results of pure RBCs and *E. coli*.
was more scattered.

Simulation details

The numerical study of acoustic pressure field and particle trajectories were implemented on the finite element software *COMSOL Multiphysics 5.5*. We used the following 2 steps to analyze separation performance of the acoustofluidic device in COMSOL:

1. Analysis of acoustic pressure field

The acoustofluidic device (including LiNbO$_3$ substrate, gold interdigital transducers, PDMS and fluids) were modeled in the section plane of microchannel (*x-z* plane) according to actual
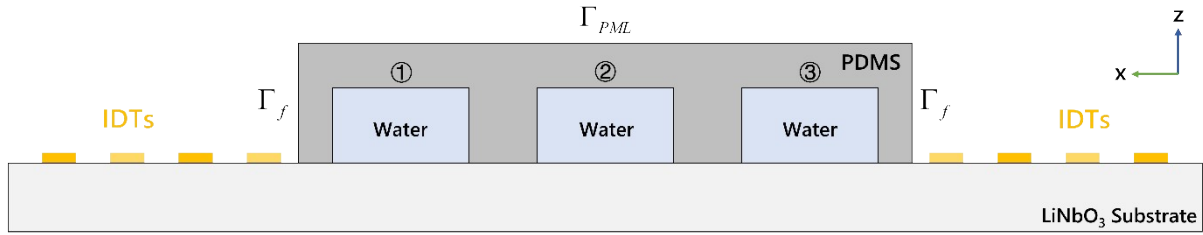
Boundary Conditions (Γ): perfect matching layer (Γ_{PML}) and free (Γ_f).

Figure S8. 2D *x-z* cross section of the serpentine acoustophoretic chip, and illustrations of simulation modeling.

geometric parameters of devices (Figure S8).

a). PDMS domain

The lid of PDMS channel are several millimeters in height. Related works demonstrated that almost all transmitted wave energy was absorbed in the PDMS, *i.e.* no waves can reflect from top boundary back to PDMS-liquid interface with the thickness of PDMS lid.[11][12] Therefore, we introduced a perfect matching layer to describe the low-reflection boundary condition. In this step, we used "Solid Mechanics" interface to describe PDMS and considered PDMS as a linear elastic material.[13] The governing equations of PDMS domain were:

$$-\rho_{PDMS}\left(1-i\mu_{PDMS}\right)\omega^2\boldsymbol{u}_s = \nabla \cdot \boldsymbol{\sigma}_s \qquad \backslash* \text{ MERGEFORMAT (1)}$$

$$\boldsymbol{\sigma}_s = \rho_{PDMS}\left[c_S^2\left(\nabla\boldsymbol{u}_s + \nabla\boldsymbol{u}_s^{T}\right) + \left(c_L^2 - 2c_S^2\right)\left(\nabla\cdot\boldsymbol{u}_s\right)\boldsymbol{I}\right] \backslash* \text{ MERGEFORMAT}$$

(2)

where $\boldsymbol{\sigma}_s$ and $\boldsymbol{u}_s$ were stress tensors and displacement field of PDMS domain, ρ_{PDMS} and μ_{PDMS} were the density and damping coefficient of PDMS,[14] c_L and c_T were the velocities of the longitudinal and shear waves in PDMS, respectively. $\boldsymbol{I}$ was the unit tensor.

b). Water domain

Inside the PDMS microchannel, water domain was modeled by "Thermoviscous Acoustics, Frequency Domain" interface. the governing equations consisted of three parts,

$$i\omega\rho_1 = -\rho_f\nabla\cdot\boldsymbol{v}_f \qquad \backslash* \text{ MERGEFORMAT (3)}$$

the continuity equation, where ρ_f and ρ_1 were the density of water and its 1st-order harmonic perturbation, and $\boldsymbol{v_f}$ was 1st-order velocity field;

$$i\omega\rho_f\boldsymbol{v}_f = \nabla\cdot\boldsymbol{\sigma}_f$$

$$\boldsymbol{\sigma}_f = -p\boldsymbol{I} + \mu_f\left(\nabla\boldsymbol{v}_f + \nabla\boldsymbol{v}_f^{\,T}\right) + \left(\eta_f + \frac{1}{3}\mu_f\right)\left(\nabla\cdot\boldsymbol{v}_f\right)\boldsymbol{I} \qquad \backslash* \text{ MERGEFORMAT}$$

(4)

the momentum equation, where $\boldsymbol{\sigma}_s$ was stress tensors of water domain μ_f and η_f were the shear and bulk viscosities of water, and p was acoustic pressure;

$$i\omega\left(\rho_f C_p T - T_0\alpha_f p_1\right) = -\nabla\cdot\left(-k_f\nabla T\right) \qquad \backslash* \text{ MERGEFORMAT (5)}$$

the energy conservation equation, where C_p, α_f and k_f were specific heat capacity, thermal expansion coefficient and thermal conductivity, respectively, and T was temperature (T_0 took the ambient value 293.15 K).

c). LiNbO$_3$ substrate and IDTs

The LiNbO$_3$ substrate and IDTs were built by "Acoustic-Piezoelectric Interaction, Frequency Domain" interface, which included "Solid Mechanics" and "Electrostatics" models. Considering piezoelectric theories were mature[14] and described in many works, the governing equations (followed *COMSOL Physics Library*) were not reiterated here. Besides, because the actual size of LiNbO$_3$ substrate is much larger than in this model, perfect matching layers are added on both sides of LiNbO$_3$ domain to ignore reflections.

d). Boundary conditions

In this model, the outer side boundaries of solid domain were both free, *i.e.,* no-stress condition for $\boldsymbol{\sigma}_s$ is applied along exterior boundaries. $\boldsymbol{n}$ was the normal vector.

$$\boldsymbol{n}\cdot\boldsymbol{\sigma}_s = \boldsymbol{0} \qquad\qquad \backslash* \text{ MERGEFORMAT (6)}$$

On the interior boundaries, continuity of velocity is implemented as a boundary condition on $\boldsymbol{v}_f$ in the fluid domain imposed by the velocity in solid domain. Considering the thermoviscous acoustic-structure boundary, the fluid-solid continuity described by

$$\boldsymbol{v}_f = i\omega\boldsymbol{u}_s,\, -\boldsymbol{n}\cdot\left(-k_f\nabla T\right) = 0 \qquad\qquad \backslash* \text{ MERGEFORMAT (7)}$$

At the solid-solid interface between PDMS and LiNbO$_3$, continuity of stress and displacement were implemented as boundary conditions.

$$\boldsymbol{u}_L = \boldsymbol{u}_s,\, \boldsymbol{\sigma}_L = \boldsymbol{\sigma}_s \qquad\qquad \backslash* \text{ MERGEFORMAT (8)}$$

where $\boldsymbol{\sigma}_L$ and $\boldsymbol{u}_L$ were stress tensors and displacement of LiNbO$_3$.

e). Mesh setup

In this simulation, each material domain was meshed by free triangular elements. To fully resolve the acoustic boundary between PDMS and water, we introduced a thin viscous boundary layer with width δ.[13]

$$\delta = \sqrt{\frac{2\eta_f}{\rho_f \cdot \omega}} = 0.15\mu m \ , \ \omega = 2\pi \cdot 12.8\text{MHz} \quad \backslash* \ \text{MERGEFORMAT (9)}$$

The maximum mesh sizes of PDMS and water domain except boundary areas were 6μm (much smaller than wavelengths of shear waves in these areas) and 3μm (20δ). Element sizes in the substrate was shorter than $\lambda/15 = 20\mu m$.

2. Particle trajectories simulation

Modeled on horizontal plane (*x-y* plane), and applied the "Laminar Flow" and "Particle Tracing" interface. In the "Particle Tracing" Module, each particle was treated as an independent particle governed by Newton's law of motion. By coupling the stokes drag field (Equation(5) in paper) with the acoustic pressure field (Equation(4) in paper) solved from analysis of acoustic pressure field, the trajectories of particles in SSAW field could be calculated. The numerical simulation result was shown in Video 1.

All relevant parameters used in the numerical study are listed in Table S2. The parameters were given at room temperature (T=293.15 K), and other unspecified parameters taken from COMSOL Material Library.

Table S2. Parameters used in numerical simulation model.[15]

Parameter	Symbol	Value
Water		
Density	ρ_f	998 kg/m^3
Shear viscosity	η_f	8.93×10^{-4} Pa·s
Bulk viscosity	μ_f	2.47×10^{-3} Pa·s
Longitudinal wave velocity	c_f	1497 m/s
Specific heat capacity	C_p	4183 J/kg·K
Thermal expansion coefficient	α_f	2.97×10^{-4} /K
Thermal conductivity	k_f	0.603 W/m·K
Compressibility	β_f	4.48×10^{-10}/Pa
Particle (Polystyrene)		
Density	ρ_p	1050 kg/m^3
Compressibility	β_p	2.59×10^{-10}/Pa
PDMS (10:1)		
Density	ρ_{PDMS}	920 kg/m^3
Longitudinal wave velocity	c_L	1030 m/s
Shear wave speed	c_S	100 m/s
Damping coefficient[13]	μ_{PDMS}	0.001
Substrate (128°Y-X LiNbO$_3$)		
Sound velocity	c_{SAW}	3953 m/s
Else		
Wavelength (set by IDTs)	λ	300 μm
Width of microchannel	W	300 μm
Height of microchannel	H	25 μm
Length of acoustic separation region	L	5 mm
Voltage amplitude	V_{pp}	36 V

Bacterial activity and function detection

To verify that this acoustofluidic separation technique can be applied to clinical testing, we tested the activity and function of bacterial cells. In subsequent testing, we set up a control group to compare with the sample after acoustofluidic separation. In the control group, sample was introduced in the same conditions, but without RF signal (SAW off).

Firstly, we made smears for *E. coil* from two groups respectively, and preformed gram staining[16] to observe their sizes and morphology. Oil immersion lens observation showed that there was no significant difference in size and morphology of bacteria (Figure S9).

Control Group   Separated Group
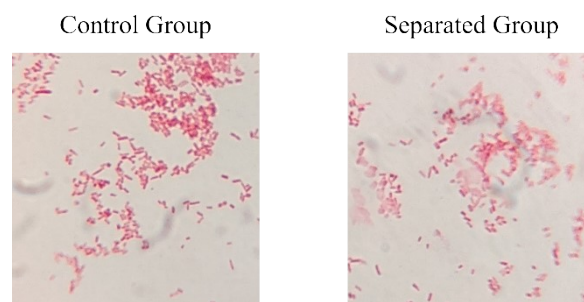
Figure S9. Under the view of microscope, the cell size and morphology of *E. coli* before and after separation.

After morphological observation, we tested the activity and function of the *E. coil* by bacterial culture and automatic microbiological biochemical analyzer (VITEK 2, bioMerieux Inc.). Diluted the sample collected from middle outlet 5×10^4 times, and took 0.5ml solution from each diluent for the inoculation on sterilized culture medium. Bacterial colonies cultured at 37℃ for 24h as shown in Figure S10. The colony number of the control group and separated group were 186 and 164, and the concentrations of *E. coil* in the corresponding samples were 1.86×10^7/mL and 1.64×10^7/mL, respectively. Considering the target cell recovery rate of the system, cell culture results demonstrated that acoustofluidic sorting did not bring an unexpected

Control Group   Separated Group
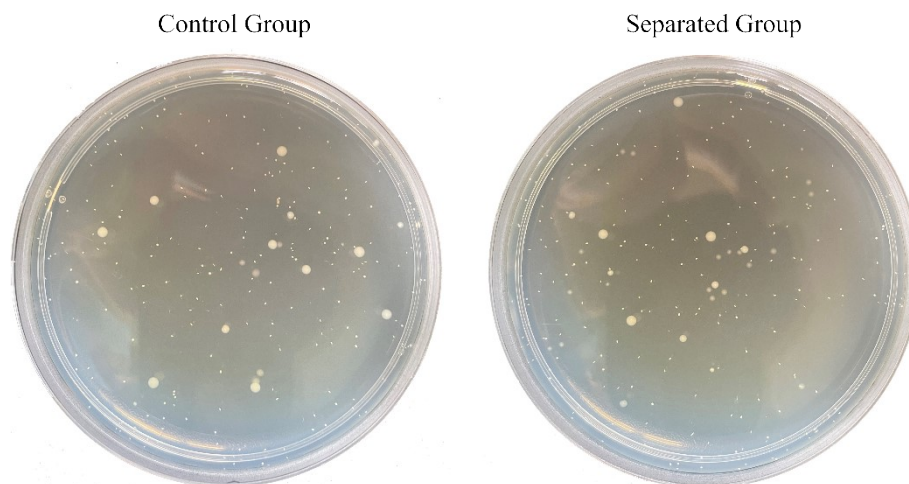
Figure S10. the bacterial colonies of control group and separated group after 24h cell culture.

effect on bacterial activity or function. In addition, *E. coli* from two groups were further qualitative analyzed by automatic microbiological biochemical analyzer, and the results demonstrated no difference in a series of biochemical test indexes. Therefore, this acoustofluidic device can maintain the activity and function of bacteria after separation.

Broader prospects

The method of increasing acoustofluidic throughput through serpentine structure is not limited to the device proposed in this paper. In addition to this design, where the pressure node lines are parallel to channel, we also applied the serpentine microchannel on taSSAW (tilted-angle standing surface acoustic wave)[5],[17] device and verified its enhancement on throughput by numerical simulation. The taSSAW device is characterized by a tilted angle θ between IDTs, or pressure node lines in SSAW field, and microchannel (Figure S10.(a)). Driven by acoustic radiation force, particles in the SSAW field tend to focus on pressure nodes and gradually move towards one side along pressure node lines(Figure S10.(b)). The numerical simulation result of particle separation using the taSSAW device is illustrated in Video 4.
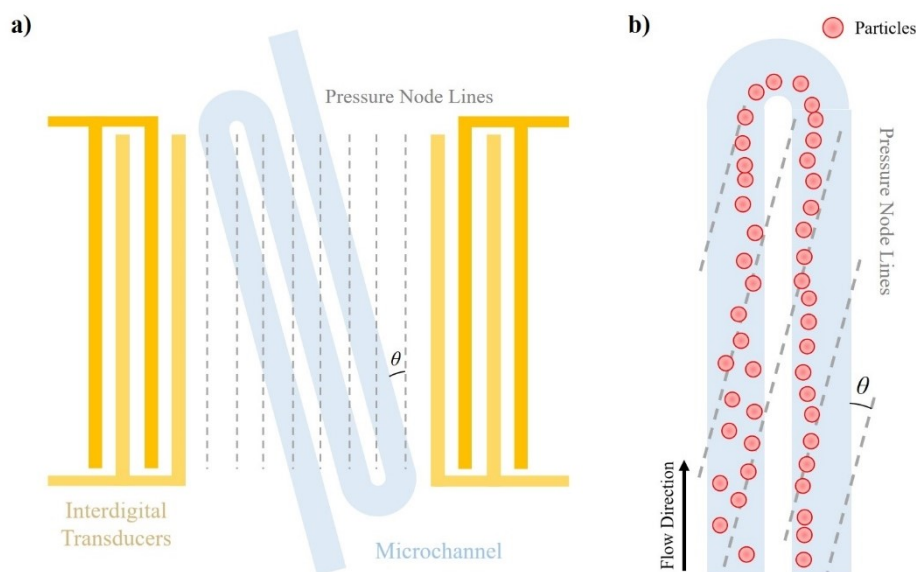
Figure S11. Design of taSSAW device with a serpentine structure. (a) Schematic of the acoustofluidic device. **(b)** Working mechanism of the acoustofluidic device.

Video 1. The numerical simulation of polystyrene particle separation in serpentine microchannel.

The simulated trajectories of 1μm and 5um polystyrene microparticles in the acoustofluidic device while SAW is on.

Video 2. The trajectory of polystyrene particles (5 μm & 1 μm) in serpentine microchannel.

Real-time video of polystyrene particles in the acoustofluidic device while SAW is on and off.

Video 3. The trajectory of cells in serpentine microchannel

Real-time video of RBCs and *E. coli* in the acoustofluidic device while SAW is on and off. In the bright-field video, *E. coli* is not visible because of its small size and high through put.

Video 4. The numerical simulation of polystyrene particle separation in taSSAW device with a serpentine structure.

The simulated trajectories of 1 μm and 5 um polystyrene microparticles in the taSSAW device while SAW is on.

References

[1] J. A. Davis, D. W. Inglis, K. J. Morton, D. A. Lawrence, L. R. Huang, S. Y. Chou, J. C. Sturm and R. H. Austin, *Proceedings of the National Academy of Sciences*, 2006, **103**, 14779-14784.

[2] M. Yamada and M. Seki, *Lab Chip*, 2005, **5**, 1233-1239.

[3] Z. Wu, B. Willing, J. Bjerketorp, J. K. Jansson and K. Hjort, *Lab Chip*, 2009, **9**, 1193-1199.

[4] Y. Ai, C. K. Sanders and B. L. Marrone, *Analytical chemistry*, 2013, **85**, 9126-9134.

[5] S. Li, X. Ding, Z. Mao, Y. Chen, N. Nama, F. Guo, P. Li, L. Wang, C. E. Cameron and T. J. Huang, *Lab Chip*, 2015, **15**, 331-338.

[6] G. Destgeer, K. H. Lee, J. H. Jung, A. Alazzam and H. J. Sung, *Lab Chip*, 2013, **13**, 4210-4216.

[7] K. Wang, W. Zhou, Z. Lin, F. Cai, F. Li, J. Wu, L. Meng, L. Niu and H. Zheng, *Sensors and Actuators B: Chemical*, 2018, **258**, 1174-1183.

[8] S. Park, Y. Zhang, T.-H. Wang and S. Yang, *Lab Chip*, 2011, **11**, 2893-2900.

[9] N. Xia, T. P. Hunt, B. T. Mayers, E. Alsberg, G. M. Whitesides, R. M. Westervelt and D. E. Ingber, *Biomedical microdevices*, 2006, **8**, 299-308.

[10] M. P. MacDonald, G. C. Spalding and K. Dholakia, *Nature*, 2003, **426**, 421-424.

[11] Z. Ni, C. Yin, G. Xu, L. Xie, J. Huang, S. Liu, J. Tu, X. Guo and D. Zhang, *Lab Chip*, 2019, **19**, 2728-2740.

[12] N. Nama, R. Barnkob, Z. Mao, C. J. Kähler, F. Costanzo and T. J. Huang, *Lab Chip*, 2015, **15**, 2700-2709.

[13] N. R. Skov and H. Bruus, *Micromachines*, 2016, **7**, 182.

[14] S. Joshi and Y. Jin, *Journal of applied physics*, 1991, **70**, 4113-4120.

[15] P. B. Muller, R. Barnkob, M. J. Jensen and H. Bruus, *Lab Chip*, 2012, **12**, 4617-4627.

[16] R. Coico, *Current protocols in microbiology*, 2006, A. 3C. 1-A. 3C. 2.

[17] S. Li, F. Ma, H. Bachman, C. E. Cameron, X. Zeng and T. J. Huang, *J Micromech Microeng*, 2017, **27**, 015031.